Additive Manufacturing 60 (2022) 103238

Contents lists available at ScienceDirect

Additive Manufacturing

journal homepage: www.elsevier.com/locate/addma

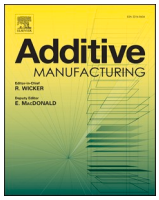

Machine learning based lattice generation method derived from topology optimisation

Jier Wang, Ajit Panesar *

Department of Aeronautics, Imperial College London, SW7 2AZ, UK

ARTICLE INFO

Keywords:
Graded lattices
Topology optimisation
Machine learning
Inverse lattice generator

ABSTRACT

Lattice structures are widely being employed in various lightweighting and multifunctional applications. With the developments in Additive Manufacturing (AM), lattice structures can now be fabricated with limited manufacturing constraints, which facilitates the design of lattice structures to become more flexible. In this paper, a novel lattice generation strategy is proposed to design graded lattice structures with the assistance of Machine Learning (ML). A Neural Network (NN)-based inverse lattice generator is trained to output lattice unit cells from the input of target mechanical properties. The proposed ML-based lattice generation method utilises the density distribution and stress field of low-resolution Topology Optimisation (TO) design to inform the inverse generator and produce lattice cells. The efficiency and efficacy of this method and the influence of cell types are demonstrated with the MBB-beam design case. Furthermore, the developed ML-based method is also applicable to multiple cell types.

1. Introduction

Lattice structure, as a non-stochastic category of cellular material, has been an attractive topic in structural design due to its ease of geometric control and feasibility of property customisation [1–3]. With the advantages of high strength-to-weight ratio, high robustness [4,5] and potentials in energy absorption, thermal insulation, sound attenuation, vibration isolation [6–9], lattice structure leads itself to applications in diverse fields, such as aerospace and biomedicine.

Additive Manufacturing (AM) has matured considerably over the past decades to offer further flexibility in structural designs whilst simultaneously reducing the constraints from manufacturing considerations [10–13]. Lattice structures, containing often small features and intricate details, have considerably benefitted from these developments in AM [14–17]. Despite the design flexibility afforded by AM, AM-related considerations like: support structure [18], powder removal [19] and other process-specific constraints still need being incorporated into the structural design procedure.

A range of lattice design approaches have been proposed to leverage the benefits they lend in several different scenarios. From micro-scale, as the property of lattice highly depend on its microstructural design, tuneable properties or desired functions can be realised through dedicatedly designing the microstructure of periodic lattices [20,21]. To design from the macro-scale, the ground truss structure method [22–25] is one of the earliest design methods for truss structures and truss-based lattices, where the geometry and topology of trusses can be formulated as a standard sizing problem. The design variables are usually set as the cross-sectional areas of trusses and sometimes the trusses, which are connections between nodes, can be added or deleted during the design process. Generic ground truss structure method [26–28] is a subcategory where heuristic algorithms are adopted for truss structures.

Topology Optimisation (TO), a powerful tool for the structural optimisation of continuum solids, can also be used to generate pseudo-lattice structures. Several approaches utilise the density distribution from TO to map the lattices: Lattice's ability to capture intermediate density with cell's volume fraction is utilised to map the density from un-penalised Solid Isotropic Material with Penalisation (SIMP) result [11,29], providing a feasible solution to the manufacturability problem of the greyscale TO structure. TO density distribution result was also utilised to set different radius for the vertex of the repeating truss-based unit to enhance part strength and energy absorption [30], or to calculate cross-sectional area for truss member considering neighbour elements to handle multiple loading conditions [31].

Multi-scale TO [32], where the macro- and the micro- scales are optimised simultaneously during the structural optimisation process, can generate high performance structures with optimised micro lattices.

* Corresponding author.
E-mail address: a.panesar@imperial.ac.uk (A. Panesar).

https://doi.org/10.1016/j.addma.2022.103238
Received 15 July 2022; Received in revised form 22 September 2022; Accepted 15 October 2022
Available online 19 October 2022

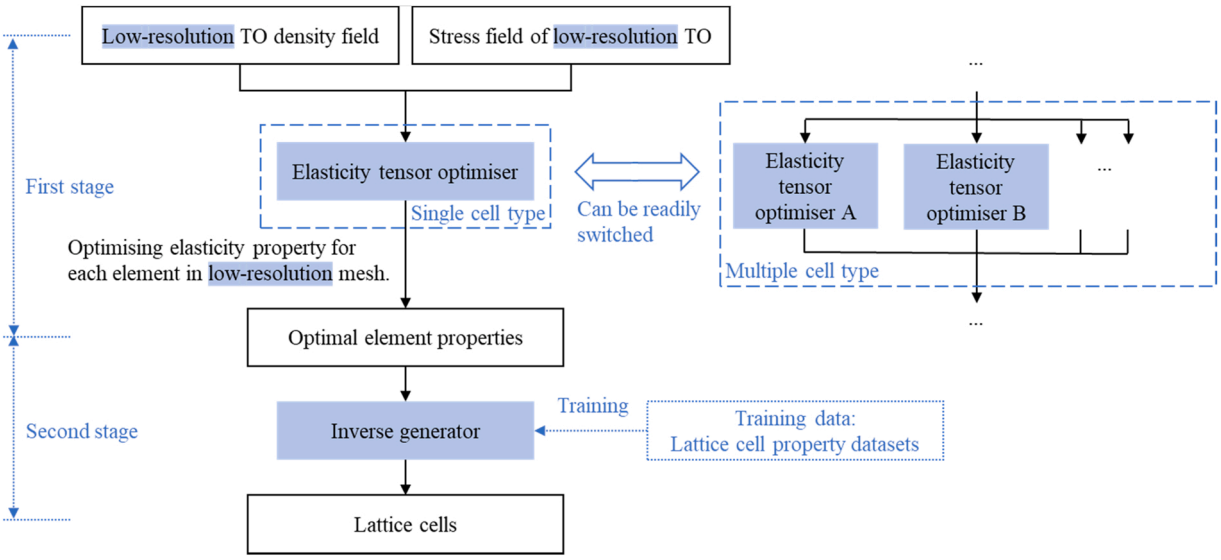

Fig. 1. Workflow of the proposed ML based lattice generation method.

Homogenisation-based multi-scale TO optimises cell parameters according to the homogenised mechanical property of lattice cells, then from the cell parameters generates the corresponding lattices [33,34]. Extension of multi-scale TO, which considers multi-topology lattices and varied strut thickness, has been applied to truss-based lattice design [35]. Further improvements like shell-infill structure [36,37], conformal patterning [38], i.e. lattice structures conforming to the shape of design region, and graded lattices connectivity [39] have been proposed to enhance multi-scale TO solutions.

Despite the above-mentioned strategies, a new branch of lattice generation methods that are supported by Machine Learning (ML) offer speed-up in the design process.

A few attempts on applying ML to lattice generation have been made and they have proven to be very effective. K-means clustering was employed to divide the meshed design domain to 3 or 4 lattice cell groups based on elemental densities followed by the micro-structure optimisation of each group [40]. Autoencoder was employed to predict mechanical properties of a microlattice using the encoder and to generate microlattices from the desired mechanical properties using the decoder [41]. One implementation of Variational Autoencoder (VAE), coupled with a mechanical property regressor is used to investigate the designs of lattice cell microstructure and multiscale lattices. The method, however, still has room for improvement on the design optimality [42]. Neural Network (NN) was deployed to establish relations between regular triangular lattice structure and its elastic properties for the design of architectured lattices with tuneable anisotropy [43]. Another attempt with NN was the establishment of data-driven inverse design where design parameters for spinodoid metamaterial were output with the input target stiffness [44]. Single-layer NN was adopted to predict the mechanical response of aniso-truss unit cell and help with the calculation of sensitivity analysis [45]. The application of ML for lattice generation is still in its infancy with great untapped potential. To this end, we propose a lattice generation strategy which derives lattice structures from TO results using the ML-based inverse generator to reduce the computation time and enhance structure performance.

This paper presents a novel ML-based lattice generation method and validates its efficiency and efficacy through a benchmark example case. The paper takes the following structure: Firstly, workflows of the proposed method are presented as a brief overview. Secondly, an introduction of graded lattice unit cell is provided, involving the parameterisation method of cell dimension and the cell elastic property considered. Thirdly, the lattice generation method, which starts with low-resolution TO result and then maps the design domain with lattice cells output from the ML model, is introduced. Finally, the well-studied MBB-beam design case is adopted as a benchmark to demonstrate the application and efficacy of this newly proposed lattice generation method with various unit cell types.

2. Methodology

2.1. Workflow of the proposed lattice generation method

As illustrated in Fig. 1, the proposed method consists of two main stages: i) obtain the optimal mechanical property for each element with the information from greyscale density solution and stress field of low-resolution TO result; ii) generate lattice unit cell which has the corresponding optimal property using the ML-based inverse generator.

When applying the ML-based method to multiple cell types (refer to the box on the right side of Fig. 1), a series of optimisers are appended to output optimal properties for different cell types, followed by a comparison between properties to determine the most suitable cell type. Advantage of this framework is that when considering multi-cell solutions, cell-specific optimisers can be made to run in parallel resulting in efficient implementation.

2.2. Lattice unit cells

2.2.1. Elastic property of lattice unit cells

The key lattice cell property considered in a compliance minimisation problem is the elasticity, which is represented using the elastic stiffness tensor $\boldsymbol{D}$. The elastic stiffness tensor $\boldsymbol{D}$ dictates the relationship between strain (ε) and stress (σ) (as Eq. (1)) and reflects how material deforms with internal stresses:

$$\boldsymbol{\sigma} = \boldsymbol{D\varepsilon} \tag{1}$$

For 2D material, the above expression can be written as:

$$\begin{bmatrix} \sigma_1 \\ \sigma_2 \\ \sigma_3 \end{bmatrix} = \begin{bmatrix} D_{11} & D_{12} & D_{13} \\ D_{21} & D_{22} & D_{23} \\ D_{31} & D_{32} & D_{33} \end{bmatrix} \begin{bmatrix} \varepsilon_1 \\ \varepsilon_2 \\ \varepsilon_3 \end{bmatrix} \tag{2}$$

where for the stress (and strain) vectors, subscript 1,2 and 3 refer to normal stress (and strain) in x direction, in y direction and shear stress (and strain).

Due to the symmetry of $\boldsymbol{D}$ matrix:

$$D_{ij} = D_{ji} \tag{3}$$

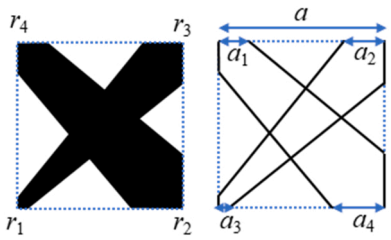

Fig. 2. Illustration of cell parameters for cell type I.

The stiffness tensor for solid material, denoted as $\boldsymbol{D}^*$, acts as a reference when compared with the stiffness tensors of lattice unit cells. For isotropic material, $\boldsymbol{D}^*$ can be calculated according to the material Young's modulus E and Poisson's ratio ν using equation:

$$\boldsymbol{D}^* = \frac{E}{1-\nu^2}\begin{bmatrix} 1 & \nu & 0 \\ \nu & 1 & 0 \\ 0 & 0 & (1-\nu)/2 \end{bmatrix} \tag{4}$$

With Young's modulus for solid material set as '1′ and Poisson's ratio as '0.3′, $\boldsymbol{D}^*$ is:

$$\boldsymbol{D}^* = \begin{bmatrix} 100/91 & 30/91 & 0 \\ 30/91 & 100/91 & 0 \\ 0 & 0 & 5/13 \end{bmatrix} \tag{5}$$

Homogenisation method is employed herein to compute the effective $\boldsymbol{D}$ for lattice unit cells. Homogenisation theory can predict the effective properties of periodic microstructures at the macroscale [46]. Although a periodic microstructure is assumed in homogenisation method, smoothly varying gradients of microstructure are allowed [47]. The aperiodic boundary condition and scale-related issues are neglected herein for computing the effective $\boldsymbol{D}$ for lattice unit cells. For detailed computational process, refer to the paper [48].

2.2.2. Cell types

In this study, three different cell types are considered to evaluate the robustness of the proposed methodology. Furthermore, the inner-cell dimensions are controlled by varying cell parameters (later on described as the parameterisation method). To visualise the structure and simplify Finite Element (FE) analysis, lattice cells are discretised into voxels. Based on the discretisation, the voxelised volume fraction of a lattice unit cell is defined as the ratio of solid voxels over total number of voxels, and is denoted as vf.

2.2.2.1. Cell type I: 2D version body-centred lattice cell. The topology of cell type I looks like an 'X′ (see Fig. 2). To determine the dimension of this cell structure, four cell parameters (r_1, r_2, r_3, r_4) numbered in counter-clockwise order are used, measuring the ratio between the length of solid rod and the cell edge length at each corner, as Eq. (6), where a represents the cell edge length.

$$\begin{aligned} r_1 &= a_1/a \\ r_2 &= a_2/a \\ r_3 &= a_3/a \\ r_4 &= a_4/a \end{aligned} \tag{6}$$

An advantage of using ratios to parameterise the cell topology is the resolution independency. Table 1 gives the elastic stiffness tensors

Table 1
Effect of resolution on cell mechanical property.

Resolution	Voxelised vf	Discretised cell	$\boldsymbol{D}$
30×30	0.7511		$\begin{bmatrix} 0.4554 & 0.2354 & 0.0000 \\ 0.2354 & 0.4554 & 0.0000 \\ 0.0000 & 0.0000 & 0.2259 \end{bmatrix}$
50×50	0.7504		$\begin{bmatrix} 0.4463 & 0.2349 & 0.0000 \\ 0.2349 & 0.4463 & 0.0000 \\ 0.0000 & 0.0000 & 0.2258 \end{bmatrix}$
100×100	0.7600		$\begin{bmatrix} 0.4556 & 0.2370 & 0.0000 \\ 0.2370 & 0.4556 & 0.0000 \\ 0.0000 & 0.0000 & 0.2299 \end{bmatrix}$
200×200	0.7550		$\begin{bmatrix} 0.4446 & 0.2354 & 0.0000 \\ 0.2354 & 0.4446 & 0.0000 \\ 0.0000 & 0.0000 & 0.2278 \end{bmatrix}$

Table 2
Examples of cell type I in resolution 100 × 100.

NO.	Cell Topology	*vf*	Cell Parameters	*D*
1	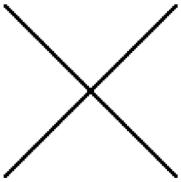	0.0976	$r_1 = 0.02$ $r_2 = 0.02$ $r_3 = 0.02$ $r_4 = 0.02$	$\begin{bmatrix} 0.0259 & 0.0258 & 0.0000 \\ 0.0258 & 0.0259 & 0.0000 \\ 0.0000 & 0.0000 & 0.0248 \end{bmatrix}$
2		0.6520	$r_1 = 0.20$ $r_2 = 0.20$ $r_3 = 0.20$ $r_4 = 0.20$	$\begin{bmatrix} 0.3141 & 0.2064 & 0.0000 \\ 0.2064 & 0.3141 & 0.0000 \\ 0.0000 & 0.0000 & 0.1882 \end{bmatrix}$
3		0.3600	$r_1 = 0.05$ $r_2 = 0.15$ $r_3 = 0.05$ $r_4 = 0.15$	$\begin{bmatrix} 0.1122 & 0.1076 & 0.0000 \\ 0.1076 & 0.1122 & 0.0000 \\ 0.0000 & 0.0000 & 0.0977 \end{bmatrix}$
4		0.4816	$r_1 = 0.205$ $r_2 = 0.065$ $r_3 = 0.215$ $r_4 = 0.075$	$\begin{bmatrix} 0.1689 & 0.1533 & 0.0646 \\ 0.1533 & 0.1671 & 0.0647 \\ 0.0646 & 0.0647 & 0.1362 \end{bmatrix}$

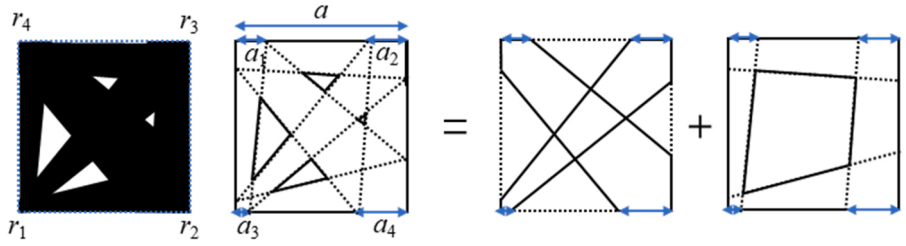

Fig. 3. Illustration of cell parameters for cell type II.

calculated for a single cell topology ($r_1 = r_2 = r_3 = r_4 = 0.25$) with four different resolutions. Both the *vf* and ***D*** vary according to the resolution option, but the variation is minimal. In the following content, the elastic stiffness tensor is calculated with resolution 100 × 100 for data collection, and regarded as constant if applied to other resolution options.

This parameterisation method permits the existence of uniform unit cells (see cell No.1 and No. 2 in Table 2), where four cell parameters are equal values, and the existence of graded unit cells (see cell No.3 and No. 4 in Table 2), where the four cell parameters govern the grading.

2.2.2.2. Cell type II: 2D version body-centred cubic lattice cell. Cell type II is generated by rods connecting every two nodes of the cell (see Fig. 3). Similar as cell type I, four nodal parameters (as formulated in Eq. (7)), which measure the lengths of solid rods over the cell length at each corner, are adopted to represent the dimension of cell type II.

$$\begin{aligned} r_1 &= a_1/a \\ r_2 &= a_2/a \\ r_3 &= a_3/a \\ r_4 &= a_4/a \end{aligned} \tag{7}$$

This parameterisation method also enables the existence of uniform unit cells (see cell No.1 and No. 2 in Table 3), where four cell parameters are equal values, and the existence of graded unit cells (see cell No.3 and No. 4 in Table 3), where the four cell parameters control the grading.

2.2.2.3. Cell type III: centre-elliptic-hole cell. Cell type III is a solid cell with an elliptic hole at the centre (see Fig. 4). Different from the above-mentioned cell type I and II, cell type III is represented by three cell parameters, where the first two parameters (r_1, r_2) define the shape of the elliptic hole and the third parameter ($0 \leq \theta \leq \frac{\pi}{2}$) defines the rotation angle of the ellipse. Eq. (8) gives the definition of r_1 and r_2, where a_1 and a_2 represents the major and minor axes of the ellipse.

$$\begin{aligned} r_1 &= a_1/a \\ r_2 &= a_2/a \end{aligned} \tag{8}$$

For cell type III, this parameterisation method allows the existence of uniform and isotropic unit cells (see cell No.1 and No. 2 in Table 4), where the first two parameters are equal values, and the existence of anisotropic and graded unit cells (see cell No. 3 and No. 4 in Table 4), where all three parameters control the anisotropy. It is of note that, when the first two parameters are equal values, the third parameter won't affect the cell structure.

Table 3
Examples of cell type II.

NO.	Cell Topology	*vf*	Cell Parameters	***D***
1	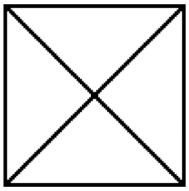	0.1352	$r_1 = 0.02$ $r_2 = 0.02$ $r_3 = 0.02$ $r_4 = 0.02$	$\begin{bmatrix} 0.0566 & 0.0163 & 0.0000 \\ 0.0163 & 0.0566 & 0.0000 \\ 0.0000 & 0.0000 & 0.0154 \end{bmatrix}$
2		0.8320	$r_1 = 0.15$ $r_2 = 0.15$ $r_3 = 0.15$ $r_4 = 0.15$	$\begin{bmatrix} 0.5981 & 0.1862 & 0.0000 \\ 0.1862 & 0.5981 & 0.0000 \\ 0.0000 & 0.0000 & 0.2156 \end{bmatrix}$
3		0.6116	$r_1 = 0.15$ $r_2 = 0.05$ $r_3 = 0.15$ $r_4 = 0.05$	$\begin{bmatrix} 0.2890 & 0.1193 & 0.0257 \\ 0.1193 & 0.2890 & 0.0257 \\ 0.0257 & 0.0257 & 0.1190 \end{bmatrix}$
4		0.4196	$r_1 = 0.60$ $r_2 = 0.03$ $r_3 = 0.07$ $r_4 = 0.08$	$\begin{bmatrix} 0.1878 & 0.0639 & 0.0055 \\ 0.0639 & 0.1855 & 0.0055 \\ 0.0055 & 0.0055 & 0.0627 \end{bmatrix}$

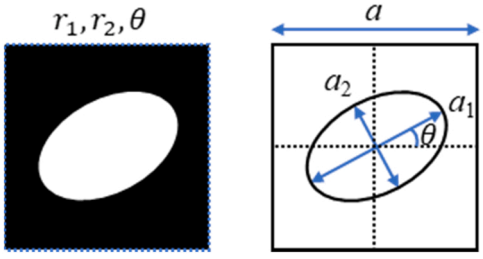

Fig. 4. Illustration of shape parameters for cell type III.

2.3. Low-resolution TO input

The overall main objective function of the lattice structural optimisation problem is to minimise the structural compliance (a measure of the inverse of stiffness). The structural compliance is defined as:

$$\boldsymbol{C} = \frac{\mathbf{1}}{\mathbf{2}}\boldsymbol{U}^{\boldsymbol{T}}\boldsymbol{K}\boldsymbol{U} \tag{9}$$

where $\boldsymbol{C}$ is the compliance, $\boldsymbol{K}$ is the global stiffness matrix and $\boldsymbol{U}$ is the global displacement vector. The structural compliance is also knowing as the total strain energy.

Solid Isotropic Material Penalisation (SIMP) method [49,50] is a density-based TO approach, which optimises the structure through redistributing the elemental densities within the design domain. Due to the ability of SIMP to indicate the optimal material distribution over design domain, the solution from SIMP (low-resolution) is utilised as the method's start point to guide lattice generation.

The objective function for SIMP is set as the structural compliance as Eq. (9), subject to a volume constraint which is defined as Eq. (10):

$$V^* - \sum_{i=1}^{N} V_i \rho_i = 0 \tag{10}$$

where V_i is the elemental volume, N is the number of elements in the design domain, V^* is the target structural volume, and ρ_i is the elemental density within the predefined region [ρ_{min}, 1].

A material interpolation scheme as Eq. (11) is used in SIMP to calculate the elastic properties of the varying elemental densities.

$$E(\rho_i) = E_0 \cdot \rho_i^p \tag{11}$$

where E_0 is the Young's modulus for solid material and p is the penalty exponent in SIMP. The value of p should be selected to precisely represent the relationship between the elastic property and the density value when the physical significance of this interpolation function is taken into consideration.

The selection of p is according to the elastic properties of lattices from dataset. Based on the converted lattice cell interpolation scheme (see Eq. (12)), a series of $D_{11}/D_{11}^* - vf$ data points are plotted in Fig. 5 for three different cell types, where D_{11} is the first entry of the elastic stiffness tensor $\boldsymbol{D}$ and D_{11}^* is the first entry of $\boldsymbol{D}^*$ for solid material. Only the uniform cells are taken into consideration for the power fitting, and D_{11} is chosen because it best correlates the volume fraction (vf) to the cell stiffness. The fitted exponential curves are also presented in Fig. 5.

$$D_{11}(vf) = D_{11}^* \cdot vf^p \tag{12}$$

For three cell types, the fitted exponents p for Eq. (12) are 2.6, 2.7 and 2.1 respectively. These values for p are adopted in SIMP as the penalty exponents. The power interpolation scheme (plotted using blue line in Fig. 5) conforms to the trend of simulation dataset and works well in practice.

Every element in the low-resolution ($nelx \times nely$) TO (SIMP) result will be filled by a lattice unit cell and the lattice cells will form the new

Table 4
Examples of cell type III.

NO.	Cell Topology	*vf*	Cell Parameters	*D*
1	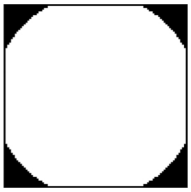	0.1308	$r_1 = 0.55$ $r_2 = 0.55$ $\theta = 0$	$\begin{bmatrix} 0.0323 & 0.0006 & 0.0000 \\ 0.0006 & 0.0323 & 0.0000 \\ 0.0000 & 0.0000 & 0.00003 \end{bmatrix}$
2		0.6148	$r_1 = 0.35$ $r_2 = 0.35$ $\theta = \pi/2$	$\begin{bmatrix} 0.4202 & 0.0825 & 0.0000 \\ 0.0825 & 0.4202 & 0.0000 \\ 0.0000 & 0.0000 & 0.0714 \end{bmatrix}$
3		0.3740	$r_1 = 0.50$ $r_2 = 0.40$ $\theta = 0$	$\begin{bmatrix} 0.2781 & 0.0086 & 0.0000 \\ 0.0086 & 0.0615 & 0.0000 \\ 0.0000 & 0.0000 & 0.0008 \end{bmatrix}$
4		0.8424	$r_1 = 0.50$ $r_2 = 0.10$ $\theta = \pi/4$	$\begin{bmatrix} 0.5080 & 0.1451 & 0.1524 \\ 0.1451 & 0.5080 & 0.1524 \\ 0.1524 & 0.1524 & 0.2143 \end{bmatrix}$

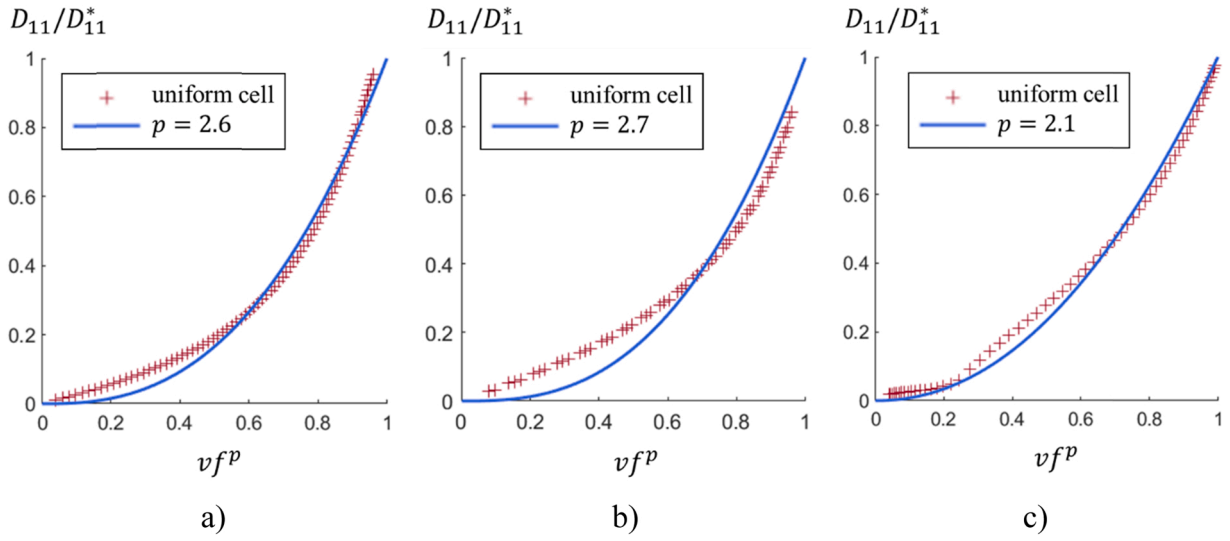

Fig. 5. $D_{11}(vf) = D_{11}^* \cdot vf^p$ power fitting. a) Cell type I, b) Cell type II, c) Cell type III.

high-resolution (*nvox* × *nvoy*) lattice structure (see Fig. 6). The relationship between these two resolutions is:

$$\begin{aligned} nvox &= res \times nelx \\ nvoy &= res \times nely \end{aligned} \tag{13}$$

where *nelx* and *nely* are the numbers of elements in x and y directions respectively in the low-resolution TO result, *nvox* and *nvoy* are the numbers of voxels in x and y directions respectively in the high-resolution structure.

2.4. Optimiser: identifying optimal elastic property

The structural optimisation objective, total strain energy, can be expressed as the sum of elemental strain energy within the whole structure:

$$SE_{total} = \sum_{element} SE_e \tag{14}$$

where SE_{total} is the total strain energy, and SE_e is the elemental strain energy.

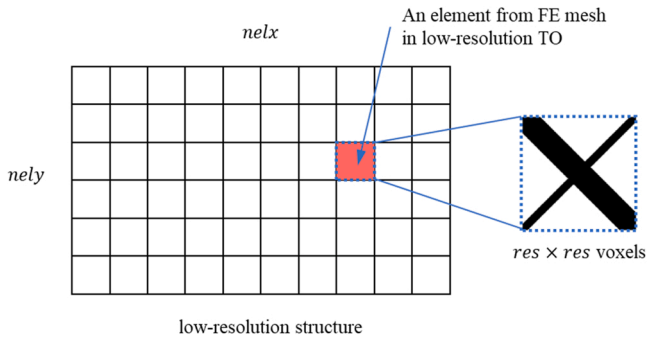

Fig. 6. Illustration of mapping lattice unit cell to each element.

Hence, when focusing on one element, the aim would be to minimise the elemental strain energy, which can be calculated by the following equation:

$$SE_e = \frac{1}{2}\boldsymbol{\varepsilon}^T\boldsymbol{\sigma} \tag{15}$$

Consider the relationship between strain $\boldsymbol{\varepsilon}$ and stress $\boldsymbol{\sigma}$ ($\boldsymbol{\sigma} = \boldsymbol{D}\boldsymbol{\varepsilon}$), the above equation can be modified as:

$$SE_e = \frac{1}{2}\boldsymbol{\sigma}^T\boldsymbol{D}^{-1}\boldsymbol{\sigma} \tag{16}$$

The elemental strain energy is then regarded as a function of $\boldsymbol{D}$. Therefore, a simple optimisation sub-problem for one element can be built with the objective defined as:

$$\min_{\boldsymbol{D}_i} : SE_e \tag{17}$$

where $\boldsymbol{D}_i$ is the elemental elastic stiffness tensor for the i-th element.

In order to implement this optimisation process, the possible region of $\boldsymbol{D}_i$ is given by a probability constraint written as:

$$P(\boldsymbol{D}_i, vf_i) \quad \geq \varepsilon \tag{18}$$

where P refers to probability, vf_i is the volume fraction of the i-th element, ε is the predefined probability limit.

This probability distribution model is built based on multi-variable Gaussian distribution model, and trained using tensors $\boldsymbol{D}$ and vf values from the same dataset for the inverse generator training.

The elemental density from SIMP result is employed to constrain the lattice cell volume fraction (vf_i) for the corresponding element position, and the constraint can be expressed as:

$$|vf_i - \rho_i(SIMP)| \leq \delta \tag{19}$$

where δ is a small variation allowed for vf_i.

To conclude, the sub-problem for each cell is defined as Eq. (20), through which the optimal elastic property for each element can be obtained

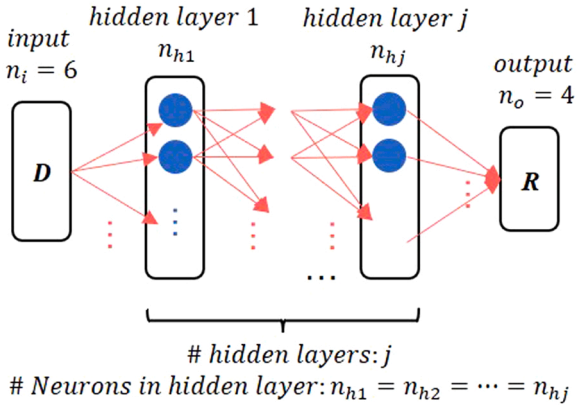

Fig. 8. Structure of the inverse generator NN.

$$\begin{aligned} &\min_{\boldsymbol{D}_i} : SE_e \\ &\text{subject to} : |vf_i - \rho_i(SIMP)| \leq \delta \\ &\quad : P(\boldsymbol{D}_i, vf_i) \geq \varepsilon \end{aligned} \tag{20}$$

In multi-cell-type cases, the above sub-problem is still applicable by using an optimiser specific to each cell type. The difference between the specific optimisers is the constraint limiting the possible region of $\boldsymbol{D}_i$ (Eq. (18)). The optimal $\boldsymbol{D}$s for all cell types are compared to determine which gives the minimum value of SE_e. After deciding the best cell type and keeping the corresponding optimal $\boldsymbol{D}$, the proposed method will move on to the next step where cell-type-specific inverse generator takes the target $\boldsymbol{D}$ as input and output the lattice cell. (Complete workflow for multi-cell-type ML-based method can be referred in Fig. 1).

2.5. Lattice mapping according to optimal elastic property

According to the optimal elastic properties obtained in the above subsection, lattice unit cells will be generated. This is achieved by a ML model referred as inverse generator (see Fig. 7), which takes the input of target elastic property and outputs the corresponding lattice unit cell which has the target elastic property. This regression problem is under the category of supervised ML. The input target elastic property is the six independent components of $\boldsymbol{D}$ matrix: D_{11},D_{12},D_{13},D_{22},D_{23},D_{33}; and the output lattice unit cell is represented by the cell parameters $\boldsymbol{R}$. The relationship between cell topology and cell elastic property has complicated physical meanings behind it and is of high dimension, that is hard to express in low-dimensional and simple mathematical functions. Hence, ML is adopted herein to model the relationship between cell topology and cell property.

Herein, the training process of the inverse generator for cell type I is explained in detail as a reference. For cell type I, the whole dataset is collected through randomly generating cell parameters ranging from 0.02 to 0.5 and computing corresponding cell elastic property using homogenisation method. Average time for computing effective property matrix of a lattice unit cell with 100×100 pixels is 0.85 s (CPU E5–2650, 32 GB RAM). The whole dataset is then randomly shuffled and split into the training data size, validation data size and test data size

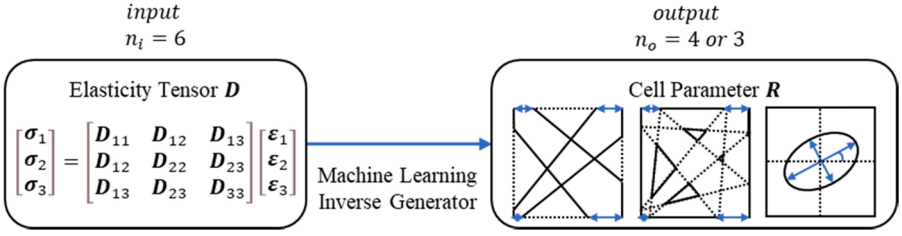

Fig. 7. Illustration of the inverse generator.

Table 5
Summary of MSE values and parameter numbers for different NN models.

Model NO.	# Hidden layers	# Neurons in hidden layer	MSE at 100th iteration	# Total parameters
1	1	4	0.002679	52
2	1	8	0.002636	100
3	2	8	0.002637	172
4	2	16	0.002610	468
5	3	16	0.002573	740

which are of size 2k, 2k and 1k, respectively. (The dataset sizes are the same for all three cell types).

To capture the nonlinearity of the mechanical model, Neural Network with the Rectified Linear Unit (ReLU) activation function is employed. An example of the fully-connected NN structure for this inverse generator problem is shown as Fig. 8.

Two hyper parameters, the neuron number in each layer and the hidden layer number, are roughly assessed using the validation dataset to obtain high-accuracy NN model within reasonable training time. The total parameter numbers are presented in Table 5 to indicate the complexity and training effort of different NN structures. To evaluate the accuracy of inverse generator model, Mean Squared Error (MSE), which is selected as the loss function of training process, is adopted to inform the model prediction accuracy (also summarised in Table 5). To visualise the training process and avoid overfitting, learning curves for different NN models are plotted in Fig. 9, which indicate that validation metric begins to stagnate at iteration 100 and all models are not overfitted.

Models *1* to *5*, the NN structures have increased numbers of total parameters. However, from Model *2* onwards, the increase of model complexity (around 2× times increment in total parameter number between neighbour models) doesn't contribute much to the model accuracy (MSE value fluctuates around 0.0026). Therefore, considering the trade-off between training time and accuracy, the final adopted inverse generator structure is a 3-layer NN (1 hidden layer) with 8 neurons in hidden layer.

To provide an insight into the performance of the selected 3-layer-NN-based inverse generator, test results (by test dataset) presented herein consist of:

i) The pixel-by-pixel comparison (presented in Fig. 10) between the original cell topology (from test dataset) and the output cell topology (from inverse generator); It is evident that the output cells look very similar as the corresponding original cells. Although slight disparity can be observed in some cases, this is due to the fact that minor variants in cell topology sometimes have neglectable effect on cell mechanical property.

ii) The quantitative comparison (presented in Fig. 11) between the input target property and the property of output cells with respect to the six independent entries of $\boldsymbol{D}$. With the target property showing on x axis and real property showing on y axis, most data points lay very close to the diagonal line, which indicates the accuracy of the trained inverse generator.

Benefitted from the simple and clear structure of the NN-based inverse generator, average time for running the inverse generator 1k times is around 2.9 s (CPU E5–2650, 32 GB RAM).

3. Case study

Some studies [36,37] concerning structural optimisation methods consider the classic Messerschmitt-Bölkow-Blohm (MBB)-beam (in 2D)

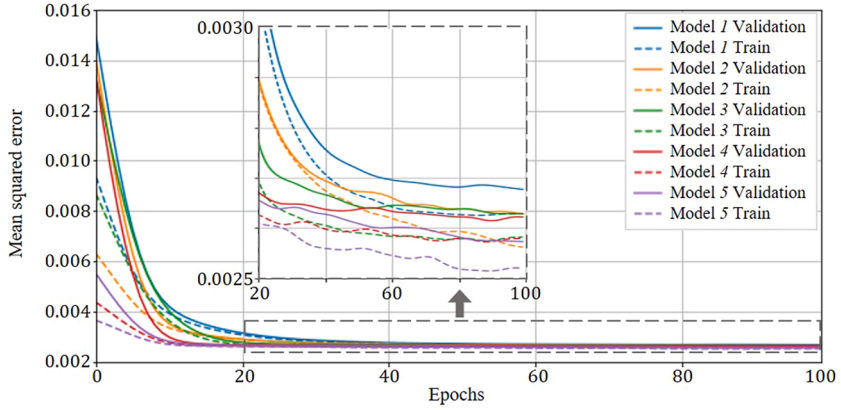

Fig. 9. Learning curves of different NN models.

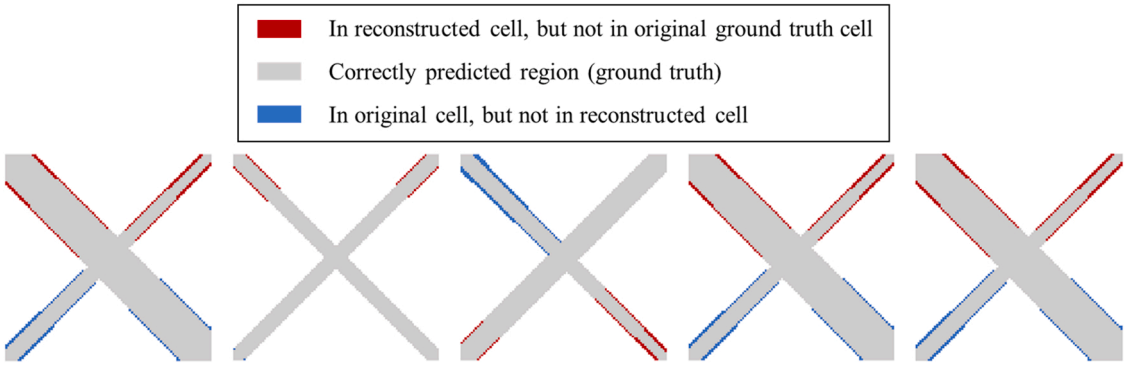

Fig. 10. Comparison between original cells and reconstructed cells.

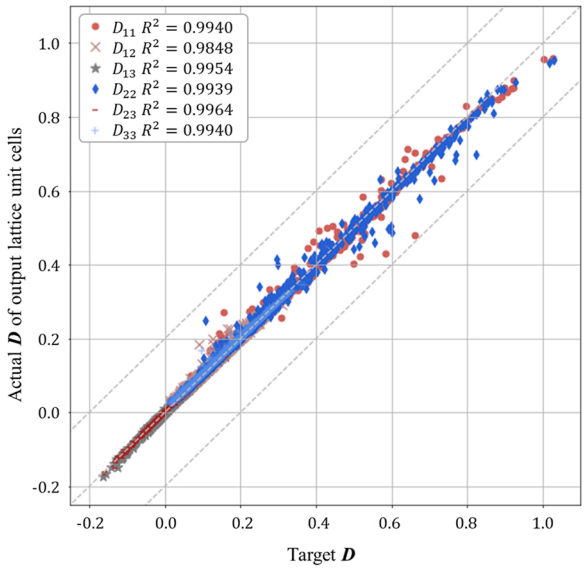

Fig. 11. ***D*** of output lattice cells vs the input target ***D***.

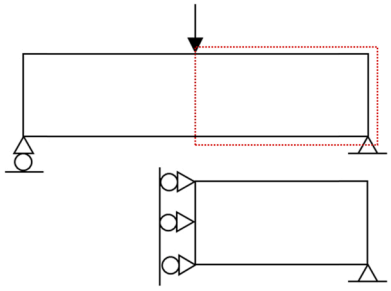

Fig. 12. The MBB-beam problem.

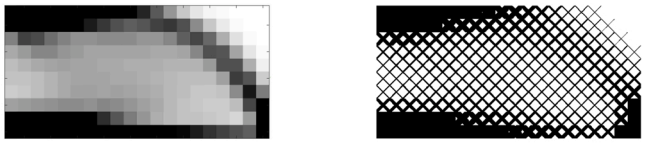

Fig. 13. Examples of a) low- and b) high- resolution structures for MBB-beam problem.

and therefore this work also utilises the same (see Fig. 12) to investigate the proposed lattice generation method. Half MBB-beam is set as the design domain of 2000 × 1000 pixels with the total volume fraction of 0.5.

For obtaining lattice structures of 2000 × 1000 pixels (as Fig. 13b), lattice unit cells occupying a 100 × 100 pixel square are used, resulting in structures comprising of 20 × 10 cells, which requires the basic information from a 20 × 10 element low-resolution TO (as Fig. 13a).

To assess the efficiency and efficacy of the proposed ML-based method, conventional density-based lattice mapping method [11,29] and traditional TO method [51] are adopted for comparisons. Density-based mapping method obtains lattice parameters by interpolating the density values of TO results and generates lattice cells based only on the density values. Traditional TO method herein refers to the high-resolution TO method which generate high-resolution structures directly. All structures are analysed using mesh of 2000 × 1000 filling the entire design domain.

Mechanical performances are evaluated in the loading scenario with

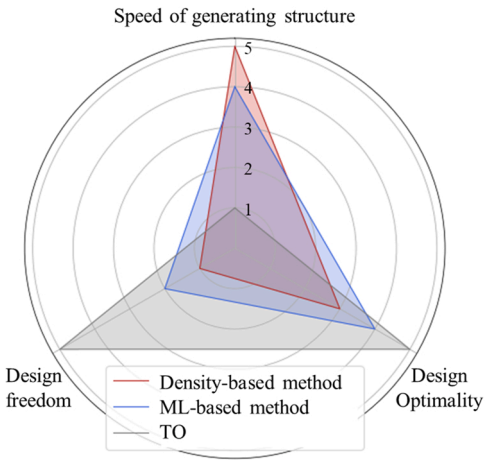

Fig. 14. Method ranking hypothesis with different criteria.

a defined loading (see Fig. 12 with a unit load vector along -y axis of $f = [0, -1]^T$). The structural compliance, which is the optimisation objective, is used as the performance measure – a lower compliance value indicates a stiffer structure.

In additional to the mechanical performance evaluation, computational effort is also considered. The latter is compared using the data (computational time) collected from *Matlab* code running on a workstation (CPU E5–2650, 32 GB RAM).

The three design methods ('ML-based', 'density-based', 'high-resolution TO') are possible to be assessed intuitively with regard to the above mentioned two aspects, and are also compared in Fig. 14, where qualitative descriptors from least to most (from 1 to 5) are used for ranking. Both design optimality and time saving can be inferred by evaluating the design freedom of each method. For example, between ML-based and density-based methods, the former one attains more design freedom by permitting the exist of 4-parameter-controlling graded lattices, whereas only single design freedom is permissible for the later. Smaller amount of design freedom can diminish the optimality of method, and reduce computational effort simultaneously.

An additional test is performed with cell type I to investigate the influence of resolution in the initial low-resolution TO step. Three different resolutions are chosen with different lattice cell sizes, which result in the same 2000 × 1000 pixel lattice structure size: i) 16 × 8 element low-resolution TO, 125 × 125 pixel lattice unit cell; ii) 20 × 10 element low-resolution TO, 100 × 100 pixel lattice unit cell; iii) 40 × 20 element low-resolution TO, 50 × 50 pixel lattice unit cell. The structural compliances are compared to demonstrate low-resolution's effect on design optimality.

4. Results and discussions

4.1. Results

Table 6 displays the lattice structures generated through both ML- and density-based methods with three cell types separately, and reports the values for structural compliance and computational time. All the designs in this section attain a total volume fraction of 0.5 with negligible difference (less than 0.002%). The reported computational time consists of the time taken to obtain the low-resolution TO design and lattice mapping.

As a benchmark design for the MBB-beam, the high-resolution TO design is shown in Table 7 together with its compliance and processing time reported.

Further implementation of the ML-based method with two different cell types (cell type I and cell type II) is reported in Table 8, as a proof of its ability to deal with multiple cell types.

Table 6
Lattice structures generated by density-based and ML-based methods.

Cell type	generation method	Lattice design	Compliance	Computational time*
Cell type I 	Density-based	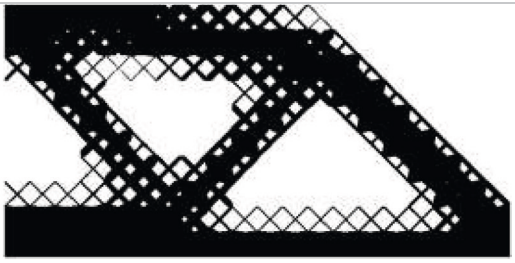	97.3	2.0s + 0.9s = 2.9s
	ML-based		94.8	2.0s + 6.1s = 8.1s
Cell type II 	Density-based	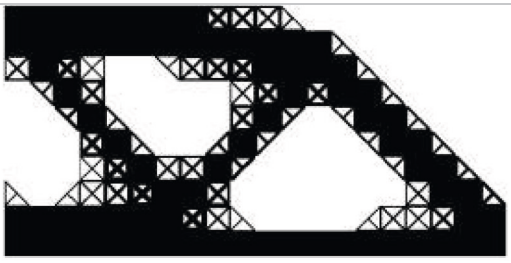	98.5	2.0s + 0.6s = 2.6s
	ML-based	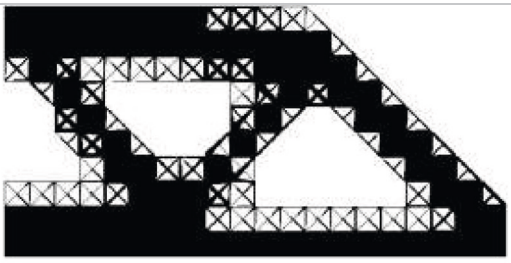	96.7	2.0s + 6.2s = 8.2s
Cell type III 	Density-based	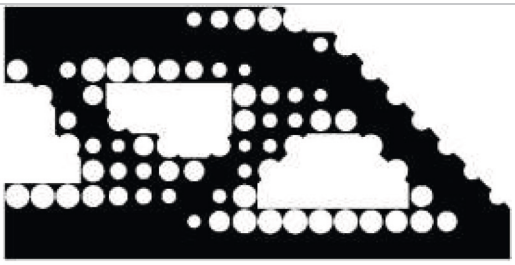	102.4	2.0s + 0.8s = 2.8s
	ML-based		96.7	2.0s + 5.0s = 7.0s

* Low-resolution TO time + lattice mapping time = total time. For ML-based method, lattice mapping time includes inferencing optimal *D* and outputting cell from *D*.

Table 7
High-resolution structural design generated by TO method.

Generation method	Design	Compliance	Computational time
TO	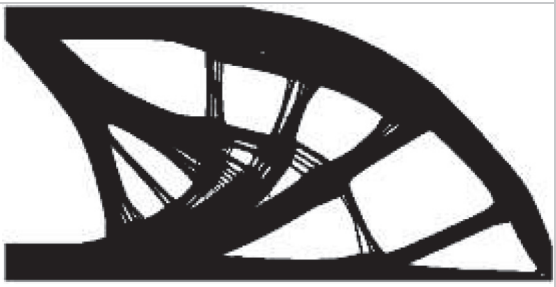	92.4	4175.1s

Table 8
Multiple-cell-type lattice structures generated by ML-based method.

Cell type	generation method	Lattice design	Compliance	Computational time*
Cell type I&II 	ML-based		94.4	2.0s + 9.3s = 11.3s

* Low-resolution TO time + lattice generation time = total time.

Additional tests on ML-based method with different resolutions in initial step (low-resolution TO) are summarised in Table 9, as a verification of low-resolution's effect.

4.2. Discussions

The ML-based method is superior (average ~3.3%) compared to density-based method in terms of mechanical performance for all the three cell types considered (refer to Table 6), which is in agreement with the intuitively hypothesised ranking of Fig. 14. This can be attributed to the consideration of stress states and the increased number of parameters in ML-based method that allows for better leveraging the high design flexibility of graded lattices. It can be expected that ML-based method would not only be superior in terms of compliance minimisation, but also for other mechanical (or functional) objectives. The design optimality of ML-based method, however, comes as an additional computational cost (average ~5 s more). As mentioned earlier, the computational time in Table 6 consists of two main parts: i) low-resolution TO, ii) lattice unit cell mapping. It should be noted that both methods initialise with the same resolution TO result (20×10), therefore the discrepancy of time for two methods seem to be directly correlated with the complexity of the unit cell mapping. The inverse generator in ML-based method, a 3-layer NN containing 8 neurons in hidden layer and requiring ~100 operations for one prediction, is marginally more demanding, as compared to the single step density-to-dimension calculation in density-based method.

Different behaviours of three cell types are also reported in Table 6, exhibiting unique characteristics. Amongst the three cell types, cell type I is observed to be the most suitable in MBB case, with the lowest compliance values. This is due to it having the most material aligned along the principle stress directions which happen to lay on the diagonals (i.e. structural members defining the topology of the cell). In terms of computational effort, the low-resolution TO processes for three cell types are expected to have the same amount of time due to the restriction on TO iterations. For density-based method, the time variance in the unit cell mapping part for three cell types is neglectable. Conversely, for ML-based method, cell type III is found to take shorter time in this part, when compared with cell type I and II. This advantage of cell type III can perhaps be attributed to the smaller number of cell parameters required to be output from inverse generator - the dimension of output can directly stack the computation amount. Besides saving time, cell type III is noticed to attain the most performance improvement (~5.6%) from density-based to ML-based method, probably due to its severe transitions from uniform to graded lattice cells.

As displayed in Table 7, high-resolution TO can produce the design with the highest performance amongst the three design methods but this comes at a tremendous computational cost. Owing to the relatively much lower resolution of preliminary TO result for ML-based method when compared to traditional TO design, a significant reduction in computational effort is found for ML-based method. Additionally, the graded lattice structure constructed by ML-based method behaves very close to the high-resolution TO design (lattice structure of cell type I is only ~2.9% inferior). When considering large-scale design problems, ML-based method can serve as a feasible alternative for traditional TO.

As discussed earlier, the proposed ML-based method can create lattice structures comprising of multiple cell types. The two-cell-type lattice structure made up of cell type I and II (refer to Table 8) shows better mechanical performance, when comparing to the single-cell-type

Table 9
Lattice structures generated by ML-based method with different low-resolutions.

Cell type	generation method	Low resolution	Cell size	Lattice design	Compliance
Cell type I 	ML-based	16 × 8	125 × 125	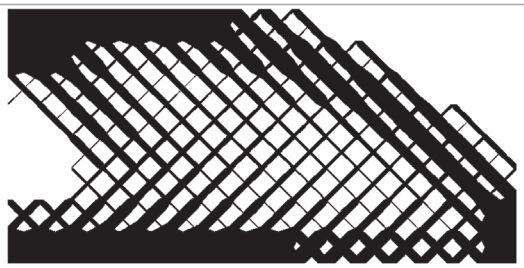	143.4
		20 × 10	100 × 100	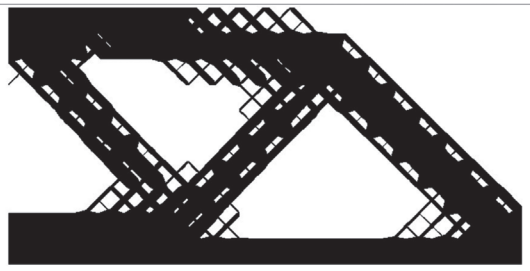	94.8
		40 × 20	50 × 50		92.2

structure, essentially because the diversity of cell types offers more options for each cell position. It can be inferred that different cell types are suitable for dissimilar loading scenarios, and adoption of apt cell types for various positions can enhance the performance. It should be noted that additional time (~3 s) is required when involving two cell types, due to the increased number of inverse generators called for each cell topology decision.

Table 9 presents the lattice structures generated from the ML-based method with varying low-resolutions in initial low-resolution TO step. When low-resolution rises, a general decreasing trend is observed for structural compliance, implying an increasing trend for structural performance. It can be attributed to the fact that finer low-resolution can offer a more detailed density distribution over the whole design domain, and lead to a higher-performance lattice structure. Whilst low-resolution 16 × 8 is a coarse mesh that the result density distribution is inadequate as a reference of lattice mapping.

5. Concluding remarks

In this paper, the potential of ML in the field of structural design was investigated for AM graded lattices. The proposed ML-based lattice generation method utilised the NN-based inverse generator as the core to map lattice cells onto low-resolution greyscale TO solutions. Besides the density solution, the stress distribution is taken into consideration to identify desired lattice properties, which (as the input) guide the inverse generator to produce optimal cells. The efficiency and efficacy of ML-based method are analysed in terms of objective performance and computational effort using the considered MBB-beam case, compared with both density-based method and traditional TO (high-resolution).

From the results obtained and presented, the following conclusions can be drawn:

The intuitive assessment of ML-based, density based and TO (pure traditional TO) methods (refer to Fig. 14), which has been verified by the result, highlights the superiority of ML-based method as the most well-rounded method. In principle, strong positive correlation with design freedom, is observed for both mechanical performance and computational effort. Lattice structures generated by ML-based method are marginally stiffer (average ~3.3%) than structures from density-based method, and only fall short (~2.5%) of the high-resolution TO designs (i.e. purely topologically optimised results). Additionally, both ML- and density-based methods, that are informed by low-resolution TO, have the advantage of time-saving, compared to high-resolution TO (saving ~99.75% time).

It is also noted that cell type plays an important role in structural performance, which concludes that different cell types are suitable for different loading cases or applications. With additional choices on cell topology, as is the case with ML-based method involving multiple cell types, a noticeable enhancement in structural performance can be seen.

The proposed ML-based method aims to inform better AM lattice designs. Lattice cell transition and connectivity would be key considerations when applying the design method to 3D lattice. Additional consideration of printability (e.g. self-supported, minimum feature size) for different AM techniques should be included in future work with experimental validation of the effectiveness of the proposed methods.

To conclude, the major findings have shown ML's enormous capability for enhancing the design optimality and design speed of lattice structural optimisation strategy, which can be expected to assist in further aspects in the field of AM structural design.

CRediT authorship contribution statement

Jier Wang: Writing – review & editing, Writing – original draft, Validation, Methodology, Investigation, Formal analysis, Conceptualization. **Ajit Panesar:** Supervision, Methodology, Conceptualization, Writing – original draft, Writing – review & editing.

Declaration of Competing Interest

The authors declare that they have no known competing financial interests or personal relationships that could have appeared to influence the work reported in this paper.

References

[1] W. Tao, M.C. Leu, Design of Lattice Structure for Additive Manufacturing, 2016. ⟨DOI: 10.1109/ISFA.2016.7790182⟩.

[2] V.S. Deshpande, N.A. Fleck, M.F. Ashby, Effective properties of the octet-truss lattice material, J. Mech. Phys. Solids vol. 49 (8) (2001) 1747–1769, https://doi.org/10.1016/S0022-5096(01)00010-2.

[3] L.J. Gibson, M.F. Ashby, Cellular Solids: Structure and Properties, second edition, 2014, pp. 1–510. ⟨DOI: 10.1017/CBO9781139878326⟩.

[4] T. Maconachie, et al., SLM lattice structures: properties, performance, applications and challenges, Mater. Des. vol. 183 (2019), https://doi.org/10.1016/j.matdes.2019.108137.

[5] M. Helou, S. Kara, Design, analysis and manufacturing of lattice structures: an overview, Int. J. Comput. Integr. Manufact. vol. 31 (3) (2017) 243–261, https://doi.org/10.1080/0951192X.2017.1407456.

[6] J. Plocher, A. Panesar, Effect of density and unit cell size grading on the stiffness and energy absorption of short fibre-reinforced functionally graded lattice structures, Addit. Manuf. vol. 33 (2020), https://doi.org/10.1016/J.ADDMA.2020.101171.

[7] T. Tancogne-Dejean, A.B. Spierings, D. Mohr, Additively-manufactured metallic micro-lattice materials for high specific energy absorption under static and dynamic loading, Acta Mater. vol. 116 (2016) 14–28, https://doi.org/10.1016/J.ACTAMAT.2016.05.054.

[8] X. Wang, T.J. Lu, Optimized acoustic properties of cellular solids, J. Acoust. Soc. Am. vol. 106 (2) (1999) 756, https://doi.org/10.1121/1.427094.

[9] P. Göransson, G. Göransson, Acoustic and vibrational damping in porous solids, Philos. Trans. R. Soc. A Math. Phys. Eng. Sci. vol. 364 (1838) (2005) 89–108, https://doi.org/10.1098/RSTA.2005.1688.

[10] J. Plocher, A. Panesar, Review on design and structural optimisation in additive manufacturing: towards next-generation lightweight structures, Mater. Des. vol. 183 (2019), https://doi.org/10.1016/j.matdes.2019.108164.

[11] D. Brackett, I. Ashcroft, R. Hague, Topology Optimization for Additive Manufacturing, 2011.

[12] J. Zhu, H. Zhou, C. Wang, L. Zhou, S. Yuan, W. Zhang, A review of topology optimization for additive manufacturing: status and challenges, Chin. J. Aeronaut. vol. 34 (1) (2021), https://doi.org/10.1016/j.cja.2020.09.020.

[13] W. Gao, et al., The status, challenges, and future of additive manufacturing in engineering, CAD Comput. Aided Des. vol. 69 (2015), https://doi.org/10.1016/j.cad.2015.04.001.

[14] L.E. Murr, S.M. Gaytan, E. Martinez, Fabricating functional Ti-alloy biomedical implants by additive manufacturing using electron beam melting, J. Biotechnol. Biomater. vol. 02 (03) (2012), https://doi.org/10.4172/2155-952x.1000131.

[15] K.C.R. Kolan, M.C. Leu, G.E. Hilmas, T. Comte, Effect of Architecture and Porosity on Mechanical Properties of Borate Glass Scaffolds Made by Selective Laser Sintering, 2013.

[16] A. Thomas, K.C.R. Kolan, M.C. Leu, G.E. Hilmas, Freeform Extrusion Fabrication of Titanium Fiber Reinforced Bioactive Glass Scaffolds, 2020.

[17] P.S. Grant, et al., Manufacture of electrical and magnetic graded and anisotropic materials for novel manipulations of microwaves, Philos. Trans. R. Soc. A Math. Phys. Eng. Sci. vol. 373 (2049) (2015), https://doi.org/10.1098/rsta.2014.0353.

[18] J. Jiang, X. Xu, J. Stringer, Support structures for additive manufacturing: a review, J. Manuf. Mater. Process. vol. 2 (4) (2018), https://doi.org/10.3390/jmmp2040064.

[19] W. Ameen, A. Al-ahmari, H. Alkhalefah, Design the support structures for easy removal of un-melted powder in metal additive manufacturing, Int. J. Adv. Manuf. Technol. vol. 29 (02) (2020).

[20] J.E. Cadman, S. Zhou, Y. Chen, Q. Li, On design of multi-functional microstructural materials, J. Mater. Sci. vol. 48 (1) (2012) 51–66, https://doi.org/10.1007/S10853-012-6643-4.

[21] O. Sigmund, Materials with prescribed constitutive parameters: an inverse homogenization problem, Int. J. Solids Struct. vol. 31 (17) (1994) 2313–2329, https://doi.org/10.1016/0020-7683(94)90154-6.

[22] M.P. Bendsøe, A. Ben-Tal, J. Zowe, Optimization methods for truss geometry and topology design, Struct. Optim. vol. 7 (3) (1994), https://doi.org/10.1007/BF01742459.

[23] S. Teufelhart, G. Reinhart, Optimization of Strut Diameters in Lattice Structures, 2012.

[24] U. Kirsch, Optimal topologies of truss structures, Comput. Methods Appl. Mech. Eng. vol. 72 (1) (1989), https://doi.org/10.1016/0045-7825(89)90119-9.

[25] M. Ohsaki. Optimization of Finite Dimensional Structures, 2016, https://doi.org/10.1201/ebk1439820032.

[26] T. Zegard, G.H. Paulino, GRAND — ground structure based topology optimization for arbitrary 2D domains using MATLAB, Struct. Multidiscip. Optim. vol. 50 (5) (2014), https://doi.org/10.1007/s00158-014-1085-z.

[27] M. Gilbert, A. Tyas, Layout optimization of large-scale pin-jointed frames, Eng. Comput. vol. 20 (7–8) (2003), https://doi.org/10.1108/02644400310503017.

[28] T. Zegard, G.H. Paulino, GRAND3 — ground structure based topology optimization for arbitrary 3D domains using MATLAB, Struct. Multidiscip. Optim. vol. 52 (6) (2015), https://doi.org/10.1007/s00158-015-1284-2.

[29] A. Panesar, M. Abdi, D. Hickman, I. Ashcroft, Strategies for functionally graded lattice structures derived using topology optimisation for additive manufacturing, Addit. Manuf. vol. 19 (2018) 81–94, https://doi.org/10.1016/J.ADDMA.2017.11.008.

[30] L. Cheng, P. Zhang, E. Biyikli, J. Bai, S. Pilz, A.C. To, Integration of Topology Optimization with Efficient Design of Additive Manufactured Cellular Structures, 2020.

[31] M. Alzahrani, S.K. Choi, D.W. Rosen, Design of truss-like cellular structures using relative density mapping method, Mater. Des. vol. 85 (2015), https://doi.org/10.1016/j.matdes.2015.06.180.

[32] J. Wu, O. Sigmund, J.P. Groen, Topology optimization of multi-scale structures: a review, Struct. Multidiscip. Optim. vol. 63 (3) (2021), https://doi.org/10.1007/s00158-021-02881-8.

[33] M.P. Bendsøe, N. Kikuchi, Generating optimal topologies in structural design using a homogenization method, Comput. Methods Appl. Mech. Eng. vol. 71 (2) (1988), https://doi.org/10.1016/0045-7825(88)90086-2.

[34] K. Suzuki, N. Kikuchi, A homogenization method for shape and topology optimization, Comput. Methods Appl. Mech. Eng. vol. 93 (3) (1991), https://doi.org/10.1016/0045-7825(91)90245-2.

[35] Y. Liu, S. Zhuo, Y. Xiao, G. Zheng, G. Dong, Y.F. Zhao, Rapid modeling and design optimization of multi-Topology lattice structure based on unit-Cell library, J. Mech. Des. Trans. ASME vol. 142 (9) (2020), https://doi.org/10.1115/1.4046812.

[36] J.P. Groen, J. Wu, O. Sigmund, Homogenization-based stiffness optimization and projection of 2D coated structures with orthotropic infill, Comput. Methods Appl. Mech. Eng. vol. 349 (2019), https://doi.org/10.1016/j.cma.2019.02.031.

[37] J. Wu, A. Clausen, O. Sigmund, Minimum compliance topology optimization of shell–infill composites for additive manufacturing, Comput. Methods Appl. Mech. Eng. vol. 326 (2017), https://doi.org/10.1016/j.cma.2017.08.018.

[38] J. Nguyen, S.I. Park, D.W. Rosen, L. Folgar, J. Williams, Conformal Lattice Structure Design and Fabrication, 2012.

[39] Y. Wang, F. Chen, M.Y. Wang, Concurrent design with connectable graded microstructures, Comput. Methods Appl. Mech. Eng. vol. 317 (2017), https://doi.org/10.1016/j.cma.2016.12.007.

[40] K. Liu, A. Tovar, E. Nutwell, D. Detwiler, Towards nonlinear multimaterial topology optimization using unsupervised machine learning and metamodel-based optimization, in: Proceedings of the ASME Design Engineering Technical Conference, 2015, vol. 2B-2015. ⟨DOI: 10.1115/DETC201546534⟩.

[41] N. Després, E. Cyr, P. Setoodeh, M. Mohammadi, Deep learning and design for additive manufacturing: a framework for microlattice architecture, JOM vol. 72 (6) (2020), https://doi.org/10.1007/s11837-020-04131-6.

[42] L. Wang, Y.C. Chan, F. Ahmed, Z. Liu, P. Zhu, W. Chen, Deep generative modeling for mechanistic-based learning and design of metamaterial systems, Comput. Methods Appl. Mech. Eng. vol. 372 (2020), https://doi.org/10.1016/j.cma.2020.113377.

[43] R. Kulagin, Y. Beygelzimer, Y. Estrin, A. Schumilin, P. Gumbsch, Architectured lattice materials with tunable anisotropy: design and analysis of the material property space with the aid of machine learning, Adv. Eng. Mater. vol. 22 (12) (2020), https://doi.org/10.1002/adem.202001069.

[44] S. Kumar, S. Tan, L. Zheng, D.M. Kochmann, Inverse-designed spinodoid metamaterials, NPJ Comput. Mater. vol. 6 (1) (2020), https://doi.org/10.1038/s41524-020-0341-6.

[45] D.A. White, W.J. Arrighi, J. Kudo, S.E. Watts, Multiscale topology optimization using neural network surrogate models, Comput. Methods Appl. Mech. Eng. vol. 346 (2019), https://doi.org/10.1016/j.cma.2018.09.007.

[46] A. Bensoussan, J.-L. Lions, G. Papanicolaou. Asymptotic Analysis for Periodic Structures, 2011, https://doi.org/10.1090/chel/374.

[47] S. Zhou, Q. Li, Design of graded two-phase microstructures for tailored elasticity gradients, J. Mater. Sci. vol. 43 (15) (2008), https://doi.org/10.1007/s10853-008-2722-y.

[48] E. Andreassen, C.S. Andreasen, How to determine composite material properties using numerical homogenization, Comput. Mater. Sci. vol. 83 (2014) 488–495, https://doi.org/10.1016/J.COMMATSCI.2013.09.006.

[49] Martin Philip Bendsøe, Ole Sigmund. Topology Optimization: Theory, Methods, and Applications, second ed., 2013.

[50] M.P. Bendsøe, Optimal shape design as a material distribution problem, Struct. Optim. vol. 1 (4) (1989), https://doi.org/10.1007/BF01650949.

[51] E. Andreassen, A. Clausen, M. Schevenels, B.S. Lazarov, O. Sigmund, Efficient topology optimization in MATLAB using 88 lines of code, Struct. Multidiscip. Optim. vol. 43 (1) (2011) 1–16, https://doi.org/10.1007/S00158-010-0594-7/TABLES/3.